

## An X/Ku-Band Focusing Anisotropic Metasurface for Low Cross-Polarization Lens Antenna Application

Hai-Peng Li, Guang-Ming Wang\*, Xiang-Jun Gao, Jian-Gang Liang, and Hai-Sheng Hou

**Abstract**—An X/Ku-band flat lens antenna based on a dual-frequency anisotropic metasurface is proposed in this paper. The function of the anisotropic metasurface is to focus the incident plane waves around 10 GHz and 14 GHz on different spots. Then we place a Vivaldi antenna with its phase centers at 10 GHz and 14 GHz well matching the focal spot of the metasurface at each frequency to build a flat lens antenna. The lens antenna has a peak gain of 18.5 dB and cross-polarization levels of lower than  $-20$  dB at 10 GHz with  $-1$  dB gain bandwidth of 9.8–10.4 GHz, while it has a peak gain of 18.8 dB and cross-polarization levels of lower than  $-30$  dB at 14 GHz with the bandwidth of 13.8–14.2 GHz. Besides single working band, the antenna can simultaneously operate at 10 GHz and 14 GHz with gains of 16.2 dB and 16.5 dB, respectively. Measured results have a good agreement with the simulated ones.

### 1. INTRODUCTION

Metasurfaces, a kind of two-dimensional metamaterials [1–4], have drawn a great deal of well-deserved attention lately [5–26]. A metasurface (MS) usually consists of a set of periodic or locally non-periodic unit cells with subwavelength sizes. The MS has the characteristics of compact size, low loss and simple fabrication, and it can flexibly control the wavefront and polarization of the electromagnetic (EM) waves by properly arranging elements on the surface of the substrate. Since Yu et al. proposed the general Snell's laws using a MS containing nano-V-antennas of different shapes in the year of 2011 [5], MS has led in the golden age of development and has been widely used in the areas of focusing [6–10], anomalous refraction/reflection [11–15], spoof surface-plasmon-polariton (SPP) coupling [16], polarization control [17–24], radar cross-section (RCS) reduction [25] and multi-beam lens [26] devices.

Among them, the focusing transmission MS can transfer the incident plane wave to its focal point and vice versa. The operating sketches shown in Fig. 1 indicate that the focusing MSs can be applied to the design of high gain planar lens antenna by properly locating feed sources over the surfaces [10]. This kind of lens antenna can also be called as transmittarray [27, 28]. These focusing MSs usually have single operating band. However, there are increasing needs for dual-band high-gain antennas with relatively larger frequency ratio in the area of remote wireless communication. To achieve dual working bands, the direct idea is to design a dual-band MS unit cell. But it is very difficult to simultaneously satisfy the requirements of the phase-control with high efficiencies at two frequency bands with only one element. Another creative idea is to insert higher-frequency elements into the space of the lower-frequency elements. However, this technology has suffered from severe coupling effect between the higher- and lower-frequency elements. To decrease the coupling, the most effective way is to make the two types of elements operating at different frequencies have orthotropic polarization reactions with electromagnetic wave. Based on this idea, the design can be further simplified by designing only one unit cell which can independently control the phases of incident waves with

---

*Received 28 March 2017, Accepted 27 June 2017, Scheduled 13 July 2017*

\* Corresponding author: Guang-Ming Wang (wgming01@sina.com).

The authors are with the Air and Missile Defense College, Air Force Engineering University, Xi'an, Shaanxi Province 710051, People's Republic of China.

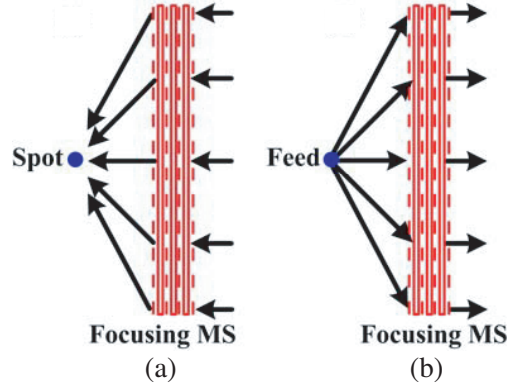


**Figure 1.** The operating sketch of (a) focusing MS and (b) lens antenna.

orthotropic polarizations and different frequencies. As long as the independent control of orthotropic polarizations is involved, we have to consider the anisotropic MS which has many applications in this area. Anisotropic MSs usually consist of unit cells which has different structures along  $x$ - and  $y$ -axes. They have great advantages in independently steering  $x$ - and  $y$ -polarization waves and can be used for designing polarization separation [17]/transformation [19–24] devices and circular polarization high gain antennas [18]. However, these devices usually require independent controls of two orthotropic polarizations at the same frequency.

In this paper, we use an anisotropic MS to realize the second idea of the dual-band flat lens antenna. Firstly, we propose a unit cell which can independently control the incident waves with different polarizations and frequencies. Secondly, we construct a dual-band anisotropic focusing MS with different focal lengths for  $x$ - and  $y$ -polarization waves and clearly verify the focusing phenomenon around 10 GHz and 14 GHz, respectively. Lastly, we use a Vivaldi antenna as a feed source to illuminate the MS. When the Vivaldi antenna is placed horizontally, vertically and obliquely, the lens antenna will operate around 10 GHz, 14 GHz, and both the frequencies, respectively. To some extent, the proposed lens antenna is polarization switchable and frequency reconfigurable. In addition, the independent control of the  $x$ - and  $y$ -polarization waves also brings about a performance of low cross-polarization levels for the proposed lens antenna.

## 2. UNIT CELL DESIGN

The structure of the MS unit cell is depicted in Fig. 2. As shown, the unit cell is multilayered with four metallic layers and three dielectric layers. The dielectric layers all have a permittivity of 2.65 and thickness of 1.5 mm. The four metallic layers are identical, and each layer contains a square ring with

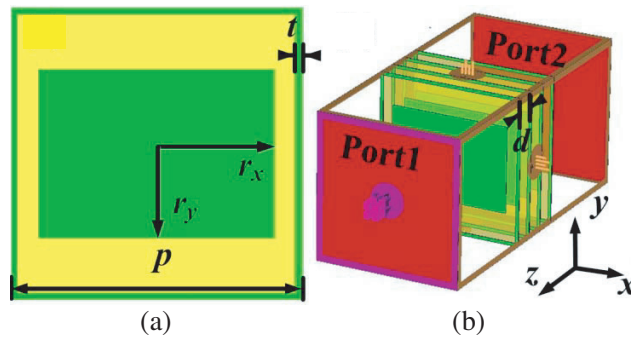


**Figure 2.** The structure and simulation setup of the unit cell. (a) Top view. (b) Perspective view with the simulation setup.  $p = 10$  mm,  $t = 0.2$  mm,  $d = 1.5$  mm.

a rectangular patch inside. For transmission MS design, it is hard to cover  $360^\circ$  phase shift range with satisfying efficiencies by single-layered structures. Multilayer stack is a valid technique to expand the phase shift range of the MS. In our design, single- and two-layer dielectric structures cannot satisfy the request of complete phase control at 10 GHz and 14 GHz. With the condition of the transmission amplitude over 0.8, the phase-steering ranges of single- and two-layer structures are  $190^\circ$  and  $290^\circ$  at 10 GHz, respectively, while they are  $130^\circ$  and  $270^\circ$  at 14 GHz, respectively. When the unit cell is three-layered, the phase-steering ranges at 10 GHz and 14 GHz are both over  $360^\circ$ . For more layers, the phase-steering range will be wider. However, more layers also mean more loss, harder fabrication and higher profile. So we adopt a three-layered structure in our design. The unit cell is simulated in CST Microwave Studio 2013 by setting periodical boundaries in  $x$ - and  $y$ -directions. The halves of the patch length and width represented by  $r_x$  and  $r_y$  respectively are selected to steer the transmission coefficients while other structure parameters remain unchanged. We can describe the transmission parameters by a matrix expressed as following:

$$T = \begin{pmatrix} T_{xx} & T_{yx} \\ T_{xy} & T_{yy} \end{pmatrix} \quad (1)$$

where  $T_{ij}$  represents the transmission coefficient under the condition that the incidence wave is  $j$ -polarized, and the transmission wave is  $i$  polarized. Owing to the axial symmetry structure of the unit cell, the cross-polarization transmission coefficients ( $T_{yx}$  and  $T_{xy}$ ) are almost equal to zero so that only the co-polarization coefficients ( $T_{xx}$  and  $T_{yy}$ ) need to be considered in the design.

We first fix the initial structure parameters as  $r_x = 4.06$  mm and  $r_y = 2.90$  mm, and the simulation phases and amplitudes of the special element are shown in Fig. 3. As can be seen, the falling edges of the passband of the amplitude curves expressed by  $\text{Am}(T_{xx})$  and  $\text{Am}(T_{yy})$  are located around 10 GHz and 14 GHz, respectively. Meanwhile, the phase curves expressed by  $\text{Arg}(T_{xx})$  and  $\text{Arg}(T_{yy})$  have a drastic decline around 10 GHz and 14 GHz, respectively.

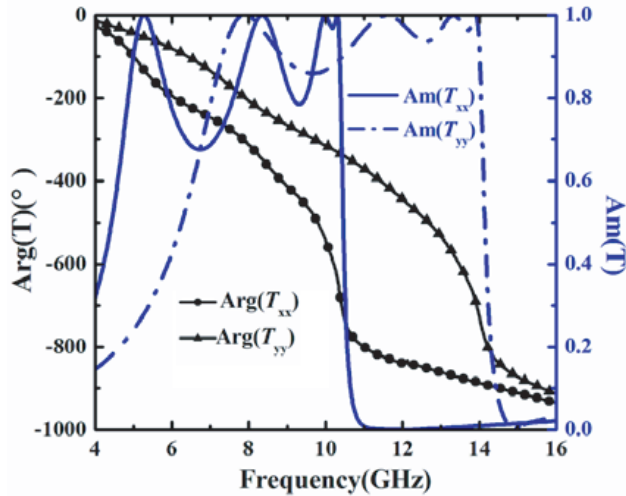


**Figure 3.** The transmission phases and amplitudes of the unit cell with structure parameters of  $r_x = 4.06$  mm,  $r_y = 2.90$  mm.

With the decrease of  $r_x$  and  $r_y$ , the passband of the amplitude curves will increase. A set of parameter values for different transmission amplitudes and phases is determined until the rising edges of the  $\text{Am}(T_{xx})$  and  $\text{Am}(T_{yy})$  curves are located around 10 GHz and 14 GHz, or the phase steering ranges already cover  $360^\circ$ . By a parameter scan with the step of 0.02 mm, the adjustment ranges for  $r_x$  of [4.06 mm, 1.2 mm] and  $r_y$  of [2.90 mm, 1.0 mm] are obtained. The curves of  $T_{xx}$  at 10 GHz and  $T_{yy}$  at 14 GHz versus  $r_x$  are plotted in Fig. 4(a). As  $r_x$  decreases from 4.06 mm to 1.2 mm,  $\text{Arg}(T_{xx})$  increases greatly with a range over  $360^\circ$  while  $\text{Arg}(T_{yy})$  changes a little. Meanwhile, the values of  $\text{Am}(T_{xx})$  at 10 GHz and  $\text{Am}(T_{yy})$  at 14 GHz are always higher than 0.8 within the whole changing range of  $r_x$ . From

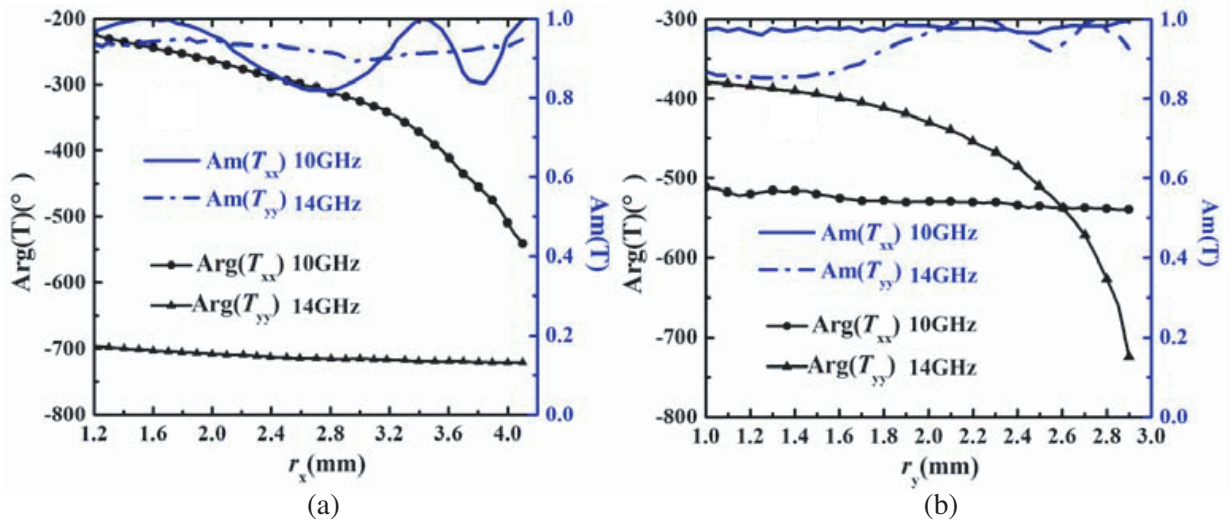


**Figure 4.** The transmission phases and amplitudes versus (a)  $r_x$  and (b)  $r_y$  at 10 GHz and 14 GHz.

Fig. 4(a), we can conclude that the phases of  $x$ -polarization incident wave can be controlled with very high transmission efficiencies and little influences on the transmission coefficients of the  $y$ -polarization incident wave just by the adjustment of  $r_x$ . For the change of  $r_y$ , the simulation results are shown in Fig. 4(b). As  $r_y$  decreases from 2.9 mm to 1.2 mm, it can be seen that  $\text{Arg}(T_{yy})$  increases greatly with a range over  $360^\circ$  while  $\text{Arg}(T_{xx})$  changes a little. In addition,  $\text{Am}(T_{xx})$  at 10 GHz and  $\text{Am}(T_{yy})$  at 14 GHz are also always higher than 0.8 within the adjustment range of  $r_y$ . By analyzing Fig. 4 comprehensively, we know that  $T_{xx}$  can be controlled by the structure parameter of  $r_x$  while  $T_{yy}$  can be well steered by  $r_y$ , and their changes have a little influence with each other. In a word, the proposed unit cell can steer  $x$ -polarization wave around 10 GHz and  $y$ -polarization wave around 14 GHz independently.

### 3. DUAL-BAND FOCUSING MS

For focusing metasurface design, the phase distribution on the surface should obey hyperbolic distribution given by Eq. (2).

$$\Phi(x, y) = \frac{2\pi}{\lambda_0}(\sqrt{x^2 + y^2 + L^2} - L) \pm 2k\pi + \Phi_0 \quad (k = 0, 1, 2, \dots) \quad (2)$$

where  $L$  is the focus length,  $\lambda_0$  the free space wavelength,  $\Phi(x, y)$  the transmission phase at the location of  $(x, y)$  on the surface, and  $\Phi_0$  the transmission phase at the referenced original point. However, the actual phase distribution on the metasurface should be discrete due to the existence of the element length. Taking the polarization characteristics of the incident wave into consideration, we can rewrite Eq. (2) as follows:

$$\text{Arg}(T_{xx})_{mn} - \text{Arg}(T_{xx})_{00} = \frac{2\pi f_x}{c}(\sqrt{(mp)^2 + (np)^2 + L_x^2} - L_x) \pm 2k\pi \quad (k = 0, 1, 2, \dots) \quad (3)$$

$$\text{Arg}(T_{yy})_{mn} - \text{Arg}(T_{yy})_{00} = \frac{2\pi f_y}{c}(\sqrt{(mp)^2 + (np)^2 + L_y^2} - L_y) \pm 2k\pi \quad (k = 0, 1, 2, \dots) \quad (4)$$

where  $m$  and  $n$  are the numbers of the unit cell on the metasurface, and they are integer.  $p$  is the length of the unit cell and  $c$  the velocity of the light. For  $x$ -polarization incident wave,  $\text{Arg}(T_{xx})_{mn}$  is the transmission phase of the unit cell numbered  $(m, n)$ ,  $\text{Arg}(T_{xx})_{00}$  the transmission phase of original element located at the center of the surface, and  $L_x$  the focal length, while for  $y$ -polarization incident wave, they are represented by  $\text{Arg}(T_{yy})_{mn}$ ,  $\text{Arg}(T_{yy})_{00}$  and  $L_y$ , respectively. In addition, the frequencies of  $x$ -polarization and  $y$ -polarization incident waves are  $f_x = 10$  GHz and  $f_y = 14$  GHz, respectively.

The settings of  $L_x$  and  $L_y$  are dependent on the phase centers of the feed antenna at 10 GHz and 14 GHz. So we need to select a proper wideband antenna as the feed source before the design of the

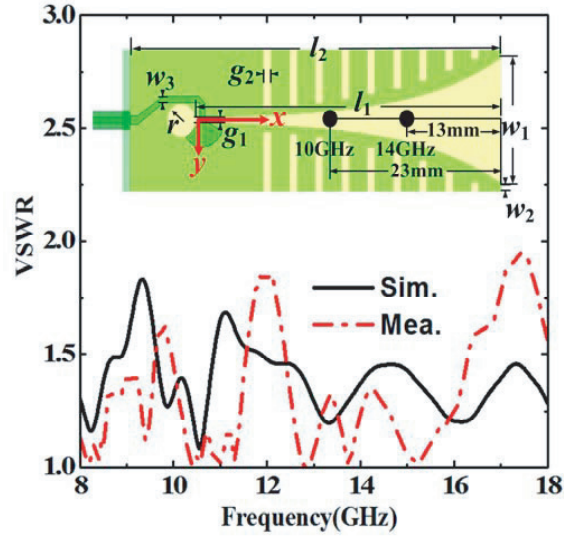


**Figure 5.** The VSWR of the Vivaldi antenna with its structure.

MS. In this work, we choose the Vivaldi antenna to illuminate the MS. Compared with other types of wideband antenna, microstrip Vivaldi antenna has the advantages of easy design and fabrication and stable farfield radiation patterns within a wide frequency band. However, the location of the phase center for the Vivaldi antenna changes with increasing frequency which needs to be compensated in the initial calculations. The structure and voltage standing wave ratios (VSWRs) of the antenna are shown in Fig. 5. The substrate has a permittivity of 2.65, thickness of 0.73 mm and loss of 0.001. The parameters of the antenna are  $w_1 = 14$  mm,  $w_2 = 1$  mm,  $w_3 = 0.95$  mm,  $l_1 = 41.2$  mm,  $l_2 = 50$  mm,  $g_1 = 0.5$  mm,  $g_2 = 1$  mm,  $r = 1.9$  mm, and the exponential curve in the structure satisfies the following equation.

$$y = \frac{g_1}{2} \exp\left(\frac{x}{l_1} \ln\left(\frac{w_1}{g_1}\right)\right) \quad (0 \leq x \leq l_1) \quad (5)$$

Compared with the simulation VSWR, the measured one is blue-shifted as a whole. This mismatch might be caused by the inhomogeneity of the substrate and fabrication inaccuracy. However, the feed antenna still satisfies VSWRs around 10 GHz and 14 GHz of lower than 2 dB. Beside this, Fig. 6 shows the simulated 3D radiation patterns at 10 GHz and 14 GHz. It is shown that both main beams point to the  $+z$ -direction at the two frequencies. Meanwhile, we should indicate that the simulation phase centers depicted in Fig. 5 are located at the distances of 23 mm and 13 mm away from the front edge of the Vivaldi antenna at 10 GHz and 14 GHz, respectively. It means that the phase centers at different frequencies have a difference of 10 mm, which is very important for fixing the MS parameters of  $L_x$  and  $L_y$  in Eq. (2) and Eq. (3). To not lose generality, we fix  $L_x = 53$  mm and  $L_y = 43$  mm according to request of 10 mm difference between 10 GHz and 14 GHz. For lens antenna design, the phase center of the feed source has to match the focus of the focusing MS. So the Vivaldi antenna has to be placed with its front edge 30 mm over the MS.

For a hyperbolic distribution given by Eq. (2), the phase increases from the original point to the around space. The unit cell shown in Fig. 3 with structure parameters of  $r_x = 4.06$  mm and  $r_y = 2.90$  mm has the smallest phase in the steering range, so we adopt it as the central and original ( $m = 0$  and  $n = 0$ ) element on the surface. By insertion of  $f_x = 10$  GHz and  $L_x = 53$  mm into Eq. (2), we can obtain the distribution of  $\text{Arg}(T_{xx})_{mn}$  on the whole MS. The distribution of  $\text{Arg}(T_{yy})_{mn}$  can also be calculated by Eq. (3) under the condition of  $f_y = 14$  GHz and  $L_y = 43$  mm. Both of the phase distributions are illustrated in Fig. 7. According to the distribution of  $\text{Arg}(T_{xx})_{mn}$ , we can find the distribution of  $r_x$  shown in Fig. 8(a) on the MS by the curve of  $\text{Arg}(T_{xx})$  versus  $r_x$  shown in Fig. 4(a). In the same way, the distribution of  $r_y$  shown in Fig. 8(b) can also be determined by the distribution of  $\text{Arg}(T_{yy})_{mn}$  shown in Fig. 7(b) and the curve of  $\text{Arg}(T_{yy})$  versus  $r_y$  shown in Fig. 4(b). Based on the parameter

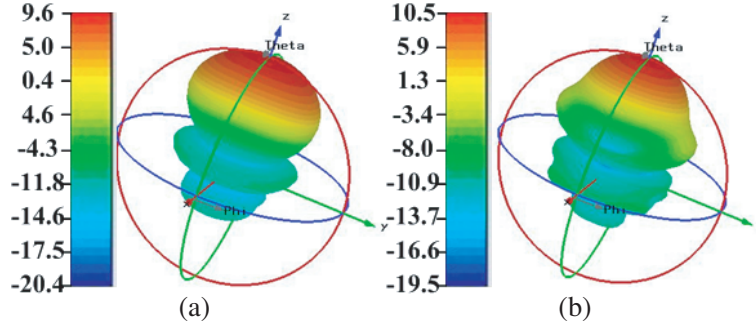


**Figure 6.** The 3D farfield radiation patterns of the Vivaldi antenna at (a) 10 GHz (b) 14 GHz.

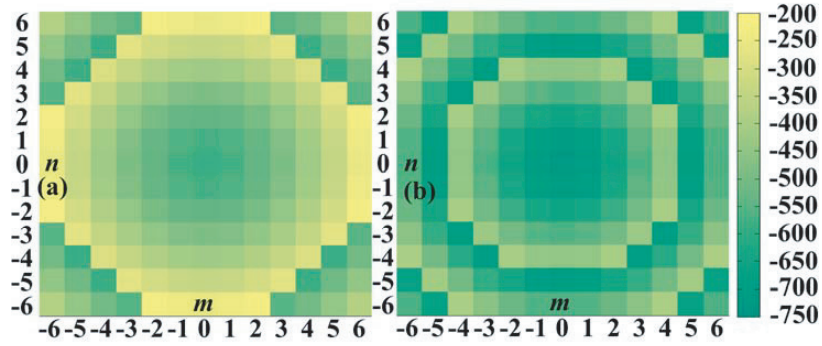


**Figure 7.** The distributions of (a)  $\text{Arg}(T_{xx})_{mn}$  at 10 GHz and  $\text{Arg}(T_{yy})_{mn}$  at 14 GHz on the whole MS.

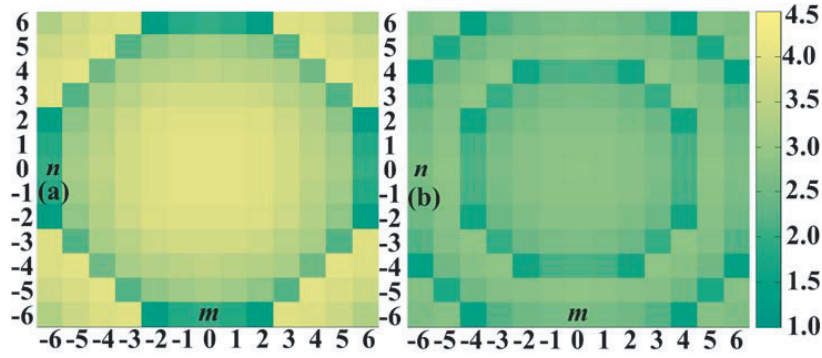


**Figure 8.** The distributions of (a)  $r_x$  and (b)  $r_y$  on the whole MS.

distributions of  $r_x$  and  $r_y$ , the simulation model of the MS can be built. Finally, the MS structure consists of  $13 \times 13$  unit cells and occupies a total area of  $130 \text{ mm} \times 130 \text{ mm}$ , shown in Fig. 9(a).

#### 4. FOCUSING PHENOMENON VERIFICATION

After the design of the dual-frequency MS, we should analyze and verify the focusing effect. A  $45^\circ$ -polarization plane-wave is used for illuminating the MS to simultaneously generate  $x$ - and  $y$ -polarization waves with equal electric field intensity. The distributions of  $x$ -component ( $E_x$ ) and  $y$ -component ( $E_y$ ) of the  $E$  field on  $xoz$ -plane at 10 GHz and 14 GHz are shown in Figs. 9(c), (d), (e) and (f), respectively. As seen from Figs. 9(c) and (f), both plane waves at 10 GHz and at 14 GHz are transformed to spherical waves across the MS. In addition, the distribution shown in Fig. 9(d) indicates that the MS has little influence on the propagation of  $y$ -polarization wave at 10 GHz while the distribution shown in Fig. 9(e)

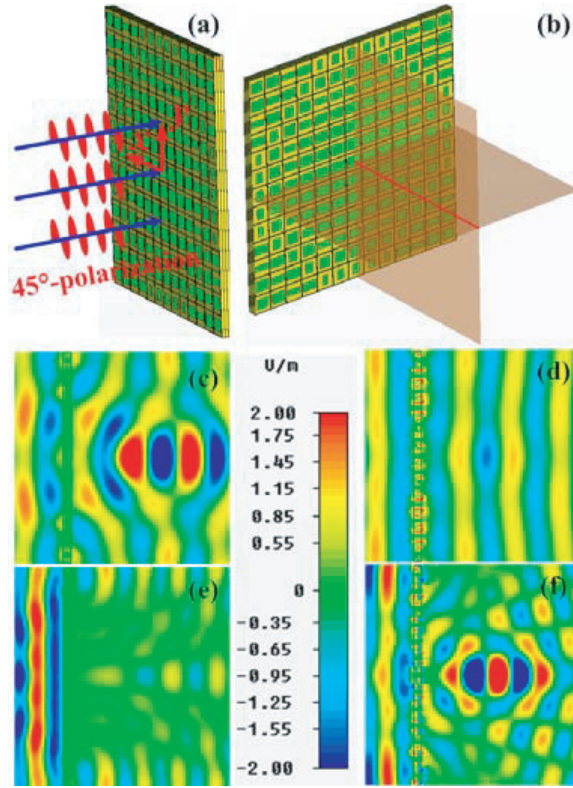


**Figure 9.** (a) Structure of the MS with the schematic of the incident wave. (b) Sketch of  $xoz$ -plane and  $yo z$ -plane with their intersection line highlighted by red color. The distributions of (c), (e)  $E_x$  and (d), (f)  $E_y$  at (c), (d) 10 GHz and (e), (f) 14 GHz.

indicates that the MS reflects most power of  $x$ -polarization wave at 14 GHz. This phenomenon has big influence on the cross-polarization radiation patterns of the Vivaldi antenna, which will be analyzed in the next part.

To describe the focusing effect more clearly, we plot the power intensity distributions at 10 GHz and 14 GHz on the two orthogonal planes in Figs. 10(a) and (b). As shown, the power intensities have been focused on two spots located in the center of a plane which is parallel to the  $xoy$ -plane for both of the distributions. In order to determine the simulation focal length (the distance of the spot at  $z$ -axis), we give the power intensity distributions along the red line marked in Fig. 9(b) at 10 GHz and 14 GHz in Figs. 10(c) and (d), respectively. As can be seen from the two figures, the peak value of the curve at 10 GHz appears at the distance of  $z = 51.8$  mm while the peak value of the curve at 14 GHz appears at the distance of  $z = 44.1$  mm. It means that the simulation values of  $L_x$  and  $L_y$  are 51.8 mm and 44.1 mm, respectively. The simulation results have a good agreement with the theoretical values of  $L_x = 53$  mm and  $L_y = 43$  mm.

### 5. X/KU BAND LENS ANTENNA DESIGN

For lens antenna design, we should place the Vivaldi antenna properly to illuminate the MS. The simulation value of  $L_x$  is 1.2 mm lower than the theoretical value while the simulation value of  $L_y$  is 1.1 mm higher than its theoretical value. The real location of the Vivaldi antenna cannot satisfy the two simulation values at the same time. Nevertheless, the differences between the simulated and theoretical values are very small so that we still place the feed antenna according to the initial setting with its front edge 30 mm over the MS. When the front edge (direction of the  $E$  field) of the Vivaldi is parallel to the  $x$ -axis, the lens antenna operates around 10 GHz, and its 3D radiation pattern is shown in Fig. 11(a).

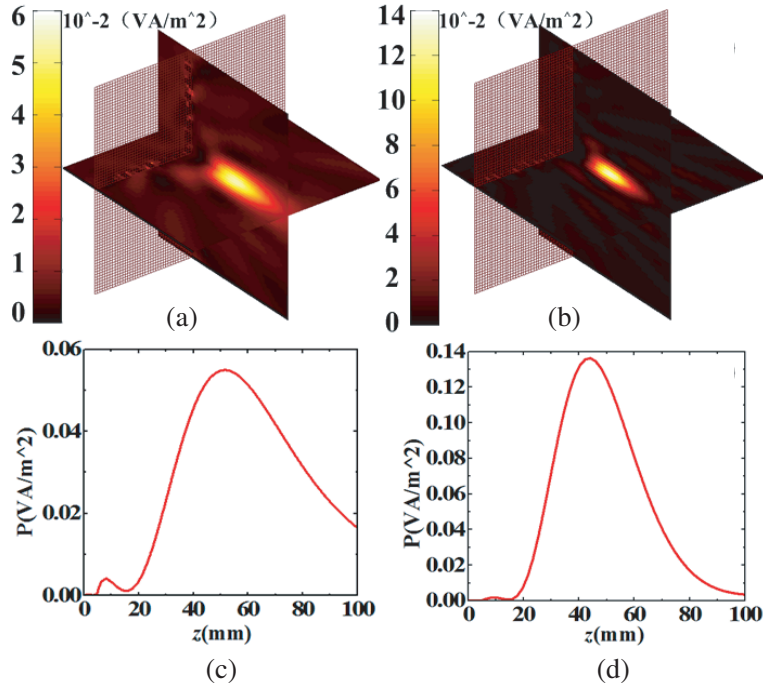


**Figure 10.** The power density distributions on (a), (b) two orthotropic planes and (c), (d) the intersection line at the frequencies of (a), (c) 10 GHz and (b), (d) 14 GHz.

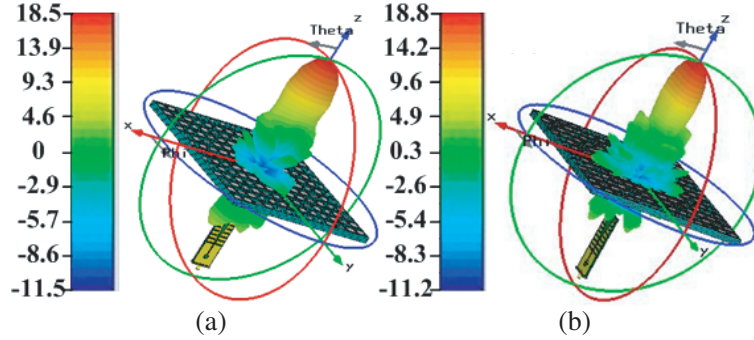


**Figure 11.** The 3D radiation patterns of the lens antenna at (a) 10 GHz, (b) 14 GHz for single (a)  $x$ -polarization and (b)  $y$ -polarization incident wave.

It is shown that the radiation pattern is pencil-shaped and has a high peak-gain of 18.5 dB. On the other hand, when the front edge is parallel to the  $y$ -axis, the lens antenna operates around 14 GHz, and its 3D radiation pattern is shown in Fig. 11(b). As shown, the radiation pattern is also pencil-shaped with a high gain of 18.8 dB. To observe the far-field results more clearly, the 2D radiation patterns of the lens antenna under the two conditions as well as the radiation patterns of the bare Vivaldi antenna are shown in Fig. 12 and Fig. 13. As shown in Fig. 12, the peak gain of the bare antenna is enhanced by 8.9 dB at 10 GHz across the MS. On the other hand, in Fig. 13, we can see that the peak gain is enhanced by 8.3 dB. Meanwhile, the lens antenna has a very narrow main beamwidth and low side-lobe levels (SLLs) at the two frequencies.

The comparison results of this work with earlier transimittarrays are shown in Table 1. It is shown that this work not only achieves dual working bands but also obtains satisfying gains with a rather small overall size. In addition, the proposed lens antenna has a characteristic of low cross-polarization

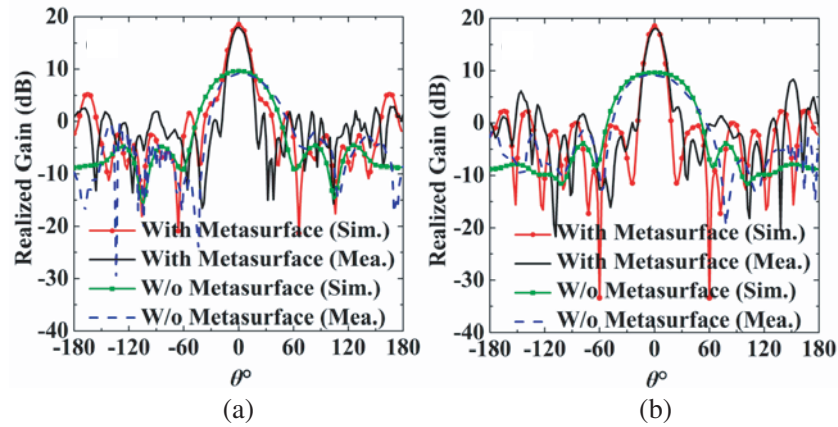


**Figure 12.** The simulated and measured 2D radiation patterns on (a) *xoz*-plane and (b) *yo<sub>z</sub>*-plane at 10 GHz.

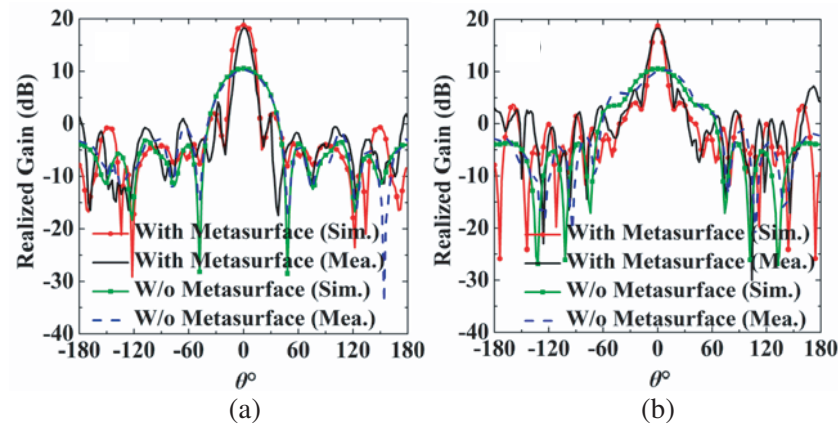


**Figure 13.** The simulated and measured 2D radiation patterns on (a) *xoz*-plane and (b) *yo<sub>z</sub>*-plane at 14 GHz.

**Table 1.** Comparison results of this work and earlier transmitarrays.

	Center frequencies (GHz)	size ( $\lambda_0 \times \lambda_0$ )	Gain (dB)
<b>Ref. 27</b>	11.3	$13.02 \times 13.02 \times 0.75$	23.76
<b>Ref. 28</b>	9.7	$6.2 \times 6.2 \times 0.039$	23
<b>Ref. 10</b>	10	$3.46 \times 3.46 \times 0.1$	16.7
<b>This work</b>	10	$4.33 \times 4.33 \times 0.15$	18.4
	14	$6.06 \times 6.06 \times 0.21$	18.8

levels at both working frequencies. As mentioned in the description of Fig. 9, the MS has different influences on the *x*- and *y*-polarization waves at 10 GHz and 14 GHz. This is different from the isotropic MS which has the same influence on different polarization incident waves. This performance will greatly decrease the cross-polarization levels of the lens antenna in our design. To verify the forecasting, we give the measured 2D radiation patterns on two orthotropic planes at 10 GHz and 14 GHz by Fig. 14. For the working frequency of 10 GHz, the MS focuses the *x*-polarization wave but has little influence on the *y*-polarization wave. The cross-polarization levels of the lens antenna at 10 GHz are decreased by approximately 9 dB within the angle range of  $[-45^\circ, 45^\circ]$  compared with the bare Vivaldi antenna.

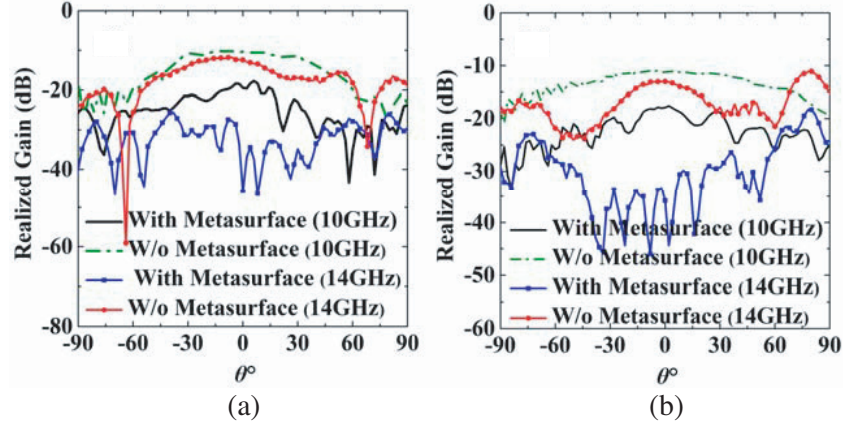


**Figure 14.** The cross-polarization radiation patterns of the lens antenna on (a)  $xoz$ -plane and (b)  $yo$  $z$ -plane.

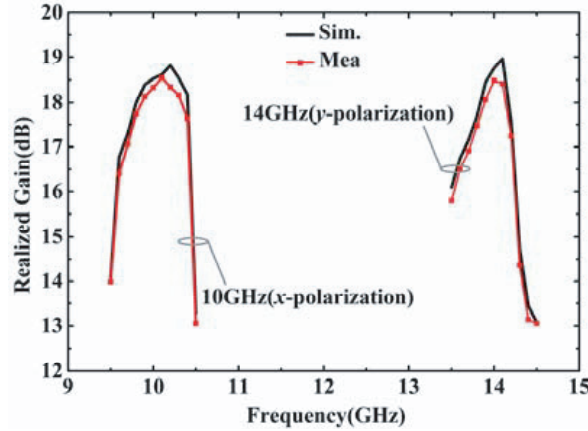


**Figure 15.** Simulated and measured gains of the lens antenna.

For the working frequency of 14 GHz, the MS not only focuses the  $y$ -polarization wave but also reflects most power of the  $x$ -polarization wave. With the effect of the two aspects, the cross-polarization levels of the lens antenna are decreased as high as 15 dB within the angle range of  $[-45^\circ, 45^\circ]$  compared with the bare Vivaldi antenna. From Fig. 14, we can also see that the cross-polarization levels with the angle range of  $[-90^\circ, 90^\circ]$  (front radiation-direction) at 10 GHz and 14 GHz are as low as  $-20$  dB and  $-30$  dB, respectively.

Besides the impedance width, we should also pay attention to the gain width of the lens antenna. The  $-1$ -dB gain width has usually been used for high-gain antenna. We give the  $-1$ -dB gain width for the lens antenna in Fig. 15. As shown, the lens antenna has a gain width of 9.8–10.4 GHz for the condition shown in Fig. 11(a) while it has a measured gain width of 13.8–14.2 GHz for the condition shown in Fig. 12(b).

The novelty of our design is that we use one MS to achieve two different focusing phase distributions. One phase distribution with the focal length of  $L_x = 53$  mm is built by the parameter distribution of  $r_x$ , and the phase distribution can be excited by  $x$ -polarization waves with the frequency around 10 GHz. Meanwhile, the phase center of the Vivaldi antenna at 10 GHz matches the focal point of the MS because of our design. So the lens antenna operates around 10 GHz when the incident wave is  $x$ -polarized. The other distribution with the focal length of  $L_y = 43$  mm is built by the parameter distribution of  $r_y$ , and this phase distribution can be excited by  $y$ -polarization waves with the frequency around 14 GHz. The phase center of the Vivaldi antenna at 14 GHz also matches the focal point of the MS in this condition. So the lens antenna operates around 14 GHz when the incident wave is  $y$ -polarized. In addition, when

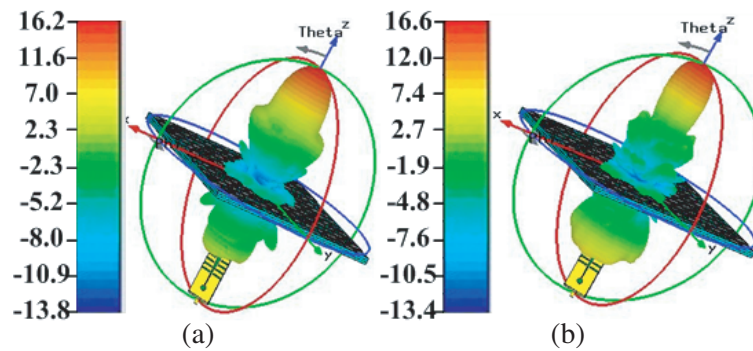


**Figure 16.** The 3D radiation patterns of the lens antenna at (a) 10 GHz, (b) 14 GHz for  $45^\circ$ -polarization incident wave.



**Figure 17.** Photographs of the (a) proposed MS and (b) its measured surroundings.

the Vivaldi antenna is placed with its front edge parallel to the diagonal of the MS, both  $x$ -polarized and  $y$ -polarized waves are omitted by the feed source. So both distributions are excited under this condition, and the lens antenna can operate at 10 GHz and 14 GHz simultaneously as shown in Fig. 16. However, the peak gains are decreased by 2.3 dB and 2.2 dB at 10 GHz and 14 GHz, respectively compared with the two conditions shown in Fig. 11. It is because the incident power is almost equally divided between  $x$ - and  $y$ -polarization incident waves. In addition, the SLLs become worse than that of the single  $x$ - or  $y$ -polarization incident wave. Finally, the samples of the MS and Vivaldi antenna are fabricated, assembled and measured. Photographs of the lens antenna and its measured surroundings are shown in Fig. 17.

## 6. CONCLUSION AND PERSPECTIVES

In conclusion, a transmitting lens antenna operating around 10 GHz and 14 GHz has been designed, fabricated and measured. The lens antenna consists of an anisotropic MS and a Vivaldi antenna. The MS has satisfying focusing effects at 10 GHz and 14 GHz, and a Vivaldi antenna with VSWRs lower than 2 dB around 10 GHz and 14 GHz is used for illuminating the MS. When the front edge of the antenna is parallel to the  $x$ -axis,  $y$ -axis and diagonal of the MS, the lens antenna can operate around 10 GHz, 14 GHz, and both frequencies. For single-band working, the lens antenna has a measured peak gain of 18.5 dB at 10 GHz with  $-1$  dB gain bandwidth of 9.8–10.4 GHz and that of 18.8 dB at 14 GHz with  $-1$  dB gain bandwidth of 13.8–14.2 GHz. The cross-polarization levels of the two frequencies are lower than  $-20$  dB and  $-30$  dB, respectively. The good performances especially for the switchable working frequency bands and the low cross-polarization levels make the lens antenna very suitable for remote satellite communication.

## ACKNOWLEDGMENT

The authors would like to express their gratitude to anonymous reviewers for their helpful comments and China North Electronic Engineering Research Institute for the fabrication. This work was supported by the National Natural Science Foundation of China (Grant No. 61372034) and the Aeronautical Science Foundation of China (Grant No. 20160196006).

## REFERENCES

1. Veselago, V. G., "The electrodynamics of substances with simultaneously negative values of  $\epsilon$  and  $\mu$ ," *Soviet Physics Uspekhi*, Vol. 10, No. 4, 509–514, 1968.
2. Pendry, J. B., A. J. Holden, D. J. Robbins, et al., "Magnetism from conductors and enhanced nonlinear phenomena," *IEEE Trans. Microw. Theory.*, Vol. 47, No. 11, 2075–2084, 1999.
3. Smith, D. R., W. J. Padilla, D. C. Vier, et al., "Composite medium with simultaneously negative permeability and permittivity," *Phys. Rev. Lett.*, Vol. 84, No. 18, 4184–4187, 2000.
4. Liu, J. P., Y. Z. Cheng, Y. Nie, and R. Z. Gong, "Metamaterial extends microstrip antenna," *Microwaves & RF*, Vol. 52, No. 12, 69–73, 2013.
5. Yu, N. F., P. Genevet, M. A. Kats, F. Aieta, J.-P. Tetienne, F. Capasso, and Z. Gaburro, "Light propagation with phase discontinuities: Generalized laws of reflection and refraction," *Science*, Vol. 334, 333–337, 2011.
6. Pors, A., M. G. Nielsen, R. L. Eriksen, and S. I. Bozhevolnyi, "Broadband focusing flat mirrors based on plasmonic gradient metasurfaces," *Nano Lett.*, Vol. 13, 829–834, 2013.
7. Xu, H. X., S. W. Tang, G. M. Wang, et al., "Multifunctional microstrip array combining a linear polarizer and focusing metasurface," *IEEE Trans. Antennas Propag.*, Vol. 64, No. 8, 3676–3282, 2016.
8. Li, X., S. Y. Xiao, B. G. Cai, Q. He, T. J. Cui, and L. Zhou, "Flat metasurfaces to focus electromagnetic waves in reflection geometry," *Opt. Lett.*, Vol. 37, 4940–4942, 2012.
9. Aieta, F., P. Genevet, M. A. Kats, N. F. Yu, R. Blanchard, Z. Gaburro, and F. Capasso, "Aberration-free ultrathin flat lenses and axicons at telecom wavelengths based on plasmonic metasurfaces," *Nano Lett.*, Vol. 12, 4932–4936, 2012.
10. Li, H.-P., G. M. Wang, J. G. Liang, X. J. Gao, H. S. Hou, and X. Y. Jia, "Single-layer focusing gradient metasurface for ultrathin planar lens antenna application," *IEEE Trans. Antennas Propag.*, Vol. 65, No. 3, 1452–1457, 2017.
11. Ni, X., N. K. Emani, A. V. Kildishev, A. Boltasseva, and V. M. Shalaev, "Broadband light bending with plasmonic nanoantennas," *Science*, Vol. 335, 427, 2012.
12. Zhang, K., X. M. Ding, L. Zhang, and Q. Wu, "Anomalous three-dimensional refraction in the microwave region by ultra-thin high efficiency metalens with phase discontinuities in the orthogonal directions," *New J. Phys.*, Vol. 16, 103020, 2014.
13. Sun, S. L., K. Yang, C. Wang, J. T. Cui, et al., "High-efficiency broadband anomalous reflection by gradient meta-surfaces," *Nano Lett.*, Vol. 12, 6223–6229, 2012.
14. Pfeiffer, C., N. K. Emani, A. M. Shaltout, et al., "Efficient light bending with isotropic metamaterial Huygens' surfaces," *Nano Lett.*, Vol. 14, No. 5, 2491–2497, 2014.
15. Monticone, F., N. M. Estakhri, and A. Alù, "Full control of nanoscale optical transmission with a composite metascreen," *Phys. Rev. Lett.*, Vol. 110, 203903, 2013.
16. Wu, C. J., Y. Z. Cheng, W. Y. Wang, B. He, and R. Z. Gong, "Ultra-thin and polarization-independent phase gradient metasurface for high-efficiency spoof surface-plasmon-polariton coupling," *Appl. Phys. Express*, Vol. 8, No. 12, 122001, 2015.
17. Cai, T., G. M. Wang, X. F. Zhang, et al., "Ultra-thin polarization beam splitter using 2-D transmissive phase gradient metasurface," *IEEE Trans. Antennas Propag.*, Vol. 63, No. 12, 5629–5636, 2015.

18. Li, H. P., G. M. Wang, J. G. Wang, and X. J. Gao, "Wideband multifunctional metasurface for polarization conversion and gain enhancement," *Progress In Electromagnetic Research*, Vol. 155, 115–125, 2016.
19. Song, K., Y. H. Liu, C. R. Luo, and X. P. Zhao, "High-efficiency broadband and multiband cross-polarization conversion using chiral metamaterial," *J. Phys. D: Appl. Phys.*, Vol. 47, 505104, 2014.
20. Yang, Y. M., W. Y. Wang, P. Moitra, I. I. Kravchenko, D. P. Briggs, and J. Valentine, "Dielectric meta-reflectarray for broadband linear polarization conversion and optical vortex generation," *Nano Lett.*, Vol. 14, 1394–1399, 2014.
21. Zhu, L., F.-Y. Meng, L. Dong, J.-H. Fu, F. Zhang, and Q. Wu, "Polarization manipulation based on electromagnetically induced transparency-like (EIT-like) effect," *Opt. Express*, Vol. 21, No. 26, 32100–32110, 2013.
22. Chen, H. Y., J. F. Wang, H. Ma, S. B. Qu, Z. Xu, A. X. Zhang, M. B. Yan, and Y. F. Li, "Ultra-wideband polarization conversion metasurfaces based on multiple plasmon resonances," *J. Appl. Phys.*, Vol. 115, 154504, 2014.
23. Ma, H. F., G. Z. Wang, G. S. Kong, and T. J. Cui, "Broadband circular and linear polarization conversions realized by thin birefringent reflective metasurfaces," *Opt. Mater. Express*, Vol. 4, No. 8, 1718–1724, 2014.
24. Pfeiffer, C. and A. Grbic, "Bianisotropic metasurfaces for optimal polarization control: Analysis and synthesis," *Phys. Rev. Applied*, Vol. 2, No. 4, 044011, 2014.
25. Chen, J., Q. Cheng, J. Zhao, D. S. Dong, and T. J. Cui, "Reduction of radar cross section based on a metasurface," *Progress In Electromagnetics Research*, Vol. 149, 205–216, 2014.
26. Zhang, K., X. M. Ding, D. L. Wo, F. R. Meng, and Q. Wu, "Experimental validation of ultra-thin metalenses for N-beam emissions based on transformation optics," *Appl. Phys. Lett.*, Vol. 108, 053508, 2016.
27. Abdelrahman, A. H., A. Z. Elsherbeni, and F. Yang, "Transmitarray antenna design using cross-slot elements with no dielectric substrate," *IEEE Antennas Wireless Propag. Lett.*, Vol. 13, 177–200, 2014.
28. Rahmati, B. and H. R. Hassani, "Low-profile slot transmitarray antenna," *IEEE Trans. Antennas Propag.*, Vol. 63, No. 1, 174–181, 2015.